

Current Driven Magnetization Reversal in Orbital Chern Insulators

Chunli Huang, Nemin Wei, and Allan. H. MacDonald
Department of Physics, University of Texas at Austin, Austin TX 78712
(Dated: September 13, 2022)

Graphene multilayers with flat moiré minibands can exhibit the quantized anomalous Hall effect due to the combined influence of spontaneous valley polarization and topologically non-trivial valley-projected bands. The sign of the Hall effect in these Chern insulators can be reversed either by applying an external magnetic field, or by driving a transport current through the system. We propose a current-driven mechanism whereby reversal occurs along lines in the (current I , magnetic-field B) control parameter space with slope $dI/dB = (e/h) M A_M (1 - \gamma^2)/\gamma$, where M is the magnetization, A_M is the moiré unit cell area, and $\gamma < 1$ is the ratio of the chemical potential difference between valleys along a domain wall to the electrical bias eV .

Introduction:— Magnetism in solid state system is produced by both spin and orbital electronic angular momentum, but the two constituents normally have a decidedly asymmetric relationship in which spins order spontaneously and orbital magnetism is induced parasitically by spin-orbit interactions. Current control of ordered spins is now routine in spintronics [1–4]. The recent discovery [5, 6] of spontaneous orbital order manifested by a quantum anomalous Hall effect in graphene moiré superlattice systems, and of current driven magnetization reversal in those systems, is the first demonstration of, an influence of a transport current on orbital magnetism. In this Letter we propose an experimentally testable explanation for this effect.

The quantum anomalous Hall effect, a property of insulators whose occupied bands carry a net Chern number, is common in graphene moiré superlattice systems [5–9] when the minibands are flat and the moiré band filling factor $\nu = n_e A_M$ is close to an odd integer. (Here n_e is the carrier density and A_M is the moiré unit cell area.) In magic angle twisted bilayer graphene [10] (MATBG), for example, the intriguing family of strongly correlated states in the $-4 < \nu < 4$ flat-band regime includes superconductors and Mott insulators [11–14], and also a Chern insulator state with a Hall resistance close [5, 6] to the von Klitzing constant. The quantized Hall conductance appears at $\nu = 3$ when the graphene bilayer is aligned with an adjacent hexagonal boron nitride layer, but unlike the case of magnetized topological insulators [15–17], cannot be a consequence of spin-order plus spin-orbit coupling since the latter is negligible in pristine graphene. The Chern insulator is instead thought to be a combined consequence of the non-trivial topology of moiré minibands in graphene multilayers [18–26] and momentum-space condensation [27–29] in the form of spontaneous valley polarization. Indeed, Hartree-Fock calculations [25, 30] predict that odd integer ν insulators in graphene multilayers are very often Chern insulators. We refer to these states as orbital Chern insulators (OCIs) although they break time reversal symmetry in both spin and orbital degrees of freedom, because the main observable - the anomalous Hall effect - is of orbital

origin, and because spin-order cannot be maintained at finite temperature when spin-orbit interactions are negligible. We therefore drop the spin-degree of freedom from the following discussion. The properties of OCIs are quite distinct [31] from those of spin Chern insulators [17]. From a statistical physics point of view, an OCI is an Ising ferromagnet in which the total Chern number of the occupied bands $C_{\pm} = \pm C$ can be viewed as an order parameter.

Experiments have shown that the Hall conductance of an OCI can be switched between $+Ce^2/h$ and $-Ce^2/h$, signaling a complete reversal of orbital magnetization [5, 6], by applying either an external magnetic field B and/or an electrical bias voltage V . The magnetization reversal mechanisms in conventional spin ferromagnets are relatively well established [32–34], and involve a combination of Stoner-Wohlfarth single domain switching and domain-wall depinning, driven by a combination of spin-transfer torques, spin-orbit torques, and magnetic fields. Consensus has however not yet been reached on the microscopics of orbital-magnetization reversal, although some interesting proposals have been put forward [6, 35, 36]. Here we analyze the case of current driven reversal in an OCI with a bulk that is perfectly insulating so that gapless charge excitations are present only at the sample edge and along domain walls. We find that both magnetic fields B and transport bias voltages V apply pressure to domain walls and predict that switching occurs along a line in the (current I , magnetic-field B) control parameter space with slope $dI/dB = (e/h) M A_M (1 - \gamma^2)/\gamma$, where M is the magnetization, A_M is the moiré unit cell area, and $\gamma < 1$ is the ratio of the chemical potential difference between valleys along a domain wall to the electrical bias voltage. In the following we first argue that moiré superlattice OCIs are described by an $O(3)$ field theory in which the vector order parameter characterizes the local valley polarization direction. This property allows domain pinning to be analyzed using conventional Landau-Lifshitz equations.

Valley-pseudospins in MATBG:— The valley-projected π -bands of twisted bilayer graphene are described by a low-energy continuum model [10] in

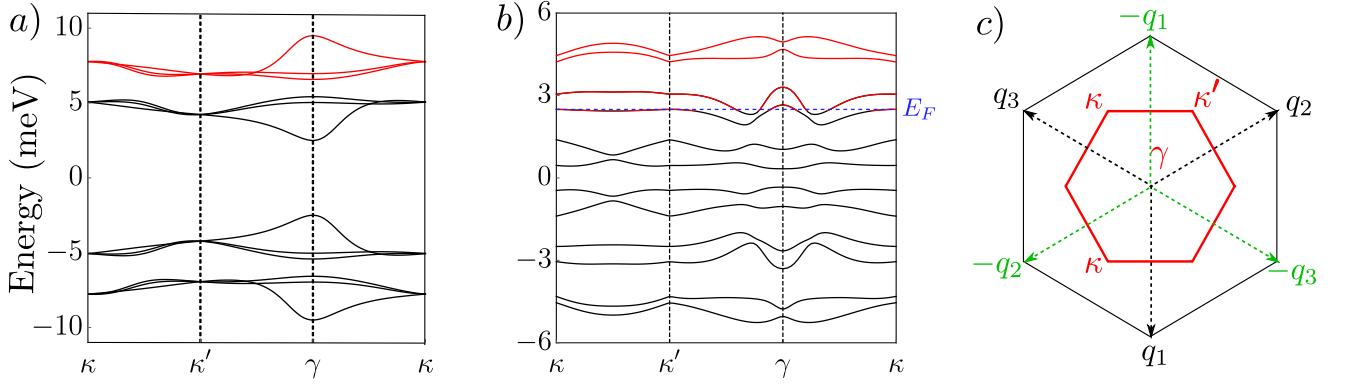


FIG. 1. Local quasiparticle bands (Eq. (5)) for a valley-exchange field pointing along a) $\hat{n} = \hat{z}$ and b) $\hat{n} = \hat{x}$. Occupied (unoccupied) states at $\nu = n_e A_M = 3$ are drawn in black (red) so that a) is an insulator while b) is a metal. For better comparison, the bands in a) have been folded into the irreducible Brillouin zone of b). Because the inter-layer tunneling terms are different in the two valleys (c) the area of the irreducible Brillouin zone (red) for general valley orientation (spanned by \mathbf{q}_1 and \mathbf{q}_2) is 1/3 of the single-particle valley-projected moiré Brillouin zones (black-solid) area (spanned by $\mathbf{q}_2 - \mathbf{q}_1$ and $\mathbf{q}_3 - \mathbf{q}_1$). These bands were calculated using spontaneous valley splitting $I = 12\text{meV}$, hBN-induced mass gap $\Delta_{\text{BN}} = 10\text{meV}$, twist angle $\theta = 1.05^\circ$, and Fermi velocity $v_F = 9.5 \times 10^5 \text{m/s}$.

which isolated layer Dirac cones are coupled by an inter-layer tunneling term that has the periodicity of the moiré pattern:

$$H_0^\tau = -i\hbar v_F(\tau\sigma_x\partial_x + \sigma_y\partial_y) - \frac{\Delta_{\text{BN}}}{2}\sigma_z|1\rangle\langle 1| + \sum_{j=1}^3 [T_j^{(\tau)} e^{-i\tau\mathbf{q}_j \cdot \mathbf{r}} |1\rangle\langle 2| + h.c.], \quad (1)$$

$$T_j^\tau = w_0\sigma_0 + w_1\sigma_x e^{\frac{2\pi i}{3}(j-1)\tau\sigma_z}, \quad (2)$$

where $\tau = \pm$ is the valley label, $|1\rangle\langle 2|$ accounts for tunneling between layers labelled 1 and 2, the σ Pauli matrices act on the sublattice degree of freedom within each layer, $\mathbf{q}_1 = (4\pi/3a_M)(0, -1)$, $\mathbf{q}_{2,3} = (4\pi/3a_M)(\pm\sqrt{3}/2, 1/2)$ and a_M is the moiré lattice constant, equal to 13.4nm at the magic angle $\theta = 1.05^\circ$. In Eq. 1 w_0, w_1 are tunneling energy parameters whose values are known. Since H_0^τ is a periodic function of position for each valley τ , it has a set of Bloch bands $H_0^\tau|u_{n\tau\mathbf{k}}\rangle = E_{n\tau}(\mathbf{k})|u_{n\tau\mathbf{k}}\rangle$ that satisfy the time-reversal symmetry property $E_{n-}(-\mathbf{k}) = E_{n+}(\mathbf{k})$, guaranteeing that the densities of states of the two-valleys are identical.

The OCI ground state at $\nu = 3$ empties the conduction band of one valley, chosen spontaneously. Mean-field calculations [25] have shown that the energy scale I of single-particle valley-flip excitations of the OCI state is $\sim 10\text{meV}$, whereas the energy scale K of long-wavelength collective valley reorientation excitations [37] $\sim 0.1 \text{meV}$. This contrast in energy scales is familiar from the properties of the conventional itinerant electron ferromagnets heavily employed in spintronics, although less extreme in the OCI case, if we identify valley in OCIs with spin in conventional ferromagnets. (In ferromagnetic Ni for example $I \sim 0.3\text{eV}$ and $K \sim 3\mu\text{eV}$ [38].) We therefore follow the approach used in metal spintronics to address

magnetization reversal by assuming that we can focus on the dynamics of the low-energy collective degrees of freedom, which are described at long wavelengths by the phenomenological micromagnetic [39] energy density:

$$\mathcal{E}[\mathbf{n}] = A(\nabla\mathbf{n})^2 - K A_M n_z^2 + K_\perp A_M \sin^2(\theta) \sin^2(\phi - \phi_p) \quad (3)$$

where $\hat{n} = (\sin\theta\cos\phi, \sin\theta\sin\phi, \cos\theta)$ is the Bloch sphere unit vector that characterizes the local collective valley spinor

$$|\Psi\rangle \sim \cos\left(\frac{\theta}{2}\right)|\tau = +\rangle + e^{i\phi}\sin\left(\frac{\theta}{2}\right)|\tau = -\rangle. \quad (4)$$

Eq. (3) is parameterized by three parameters (with dimension of energy) $A, K, K_\perp > 0$ which arise naturally from the following considerations: A is a stiffness parameter that expresses an energetic preference for uniform valley polarized states, K is a valley anisotropy constant that favors complete polarization in $|\tau = \pm\rangle$ in the OCI ground state, and K_\perp is an azimuthal anisotropy constant that accounts for processes that violate valley conservation. Since $K_\perp = 0$ is a consequence of momentum conservation in perfect crystals, we anticipate that $K_\perp \neq 0$ only near sample edges.

In Fig. 1 we plot the mean-field quasiparticle energy bands of an OCI for two different valley-orientations \hat{n} by adding an exchange field with Stoner interaction constant $I = 12 \text{meV}$ to Eq. (2)

$$H_{MF} = \frac{H_0^+ + H_0^-}{2} + \tau_z \frac{H_0^+ - H_0^-}{2} - \frac{I}{2}\boldsymbol{\tau} \cdot \mathbf{n}, \quad (5)$$

where the $\boldsymbol{\tau}$ Pauli matrices act on the valley degree of freedom. The choice of an exchange effective magnetic

field that is aligned with the valley orientation is motivated by the observation the dominant Coulomb interactions in graphene multilayers are valley-independent, just as the Coulomb interactions in a magnetic metal are spin-independent. The OCI band-structure calculation has three important messages. First, the bandstructure is independent of ϕ as a result of total valley number conservation in Eq. 5. This band model result is consistent with the expectation that $K_{\perp} = 0$ in perfect periodic lattice. Second, as \hat{n} goes from the pole (Fig. 1a) to the equator (Fig. 1b), the bandwidth decreases and total energy increases, suggesting that the easy direction of valley polarization is the polar axis in agreement with experiment. Because the exchange field couples valleys and the tunneling Hamiltonians in the two valleys are not identical, the moiré Hamiltonian unit cell area is increased (by a factor of three) when $\sin(\theta/2) \neq 0$, as illustrated in Fig. 1c. Third, we found that the local band structure is metallic when \hat{n} is close to the equator, a property that will have important implications for domain wall dynamics.

Domain Wall Dynamics:— We can calculate magnetization dynamics from Eq. 3 by recognizing that the two-components of valley pseudospin perpendicular to \hat{n} (when suitably normalized) are canonical conjugate variable. The Euler-Lagrange equation corresponding to Eq. 3 is therefore:

$$\frac{\hbar}{2A_M} \partial_t \mathbf{n} = \mathbf{n} \times \frac{\delta \mathcal{E}}{\delta \mathbf{n}} + \frac{\hbar}{2A_M} \mathbf{n} \times (\check{\alpha} \cdot \partial_t \mathbf{n}). \quad (6)$$

Eq. 6 is known in spintronics as the Landau-Lifshitz Gilbert equation and includes a damping tensor $\check{\alpha}$ that accounts for coupling between collective magnetic degree of freedom and other low-energy degrees of freedom, including phonons and gapless quasiparticle excitations if these are present. Applying Eq. 6 to Eq. 3 and linearizing around $n_z = 1$ yields the valley-wave collective mode energies $E(q) = 4K + 4AA_M q^2$. By fitting to microscopic bulk collective mode calculations [37], we estimate that $K \sim 0.04\text{meV}$ and $AA_M \sim 0.13\text{meV}a_M^2$.

A domain wall, like the one illustrated schematically in Fig. 2, is a real-space topological defect obtained by minimizing the energy functional Eq. 3 with the constraint that $n_z \rightarrow \pm 1$ for $x \rightarrow \pm\infty$. This yields $\phi = \phi_p$ and $\theta = 2 \arctan \exp(x - X/\lambda)$, where X is the domain wall center, $\lambda = \sqrt{AA_M/K}$ is half-width of the domain wall. Using the values for K and A quoted above yields $\lambda = 1.8a_M$. In order to describe wall dynamics, we use a generalization of Slonczewski's [40] *ansatz* by letting the domain wall position and azimuthal phase,

$$X = X(y, t), \quad \phi = \phi(y, t), \quad (7)$$

depend on time and the coordinate along the wall. This dynamics focuses on excitation of the *soft-mode* of a domain wall associated with its invariance under a shift in

X in the absence of pinning. In practice, domain walls are invariably pinned by sample inhomogeneities in real devices, and this pinning is responsible for hysteresis. For definiteness we assume that the domain wall is pinned at $X = 0$ by some extrinsic pinning potential E_{pin} which can arise from, *e.g.* a twist-angle extremum at which the condensation energy of the ordered state is minimized, or a local minimum in the width W of the sample. There is an energy penalty dE_{pin} to shift X away from $X = 0$. For simplicity, we take it to be specified by a harmonic potential

$$dE_{pin} = E_{pin}(X) - E_{pin}(X = 0) = \frac{kW}{2} X^2, \quad (8)$$

up to a maximum $|X| < X_{max}$ beyond which the pinning energy is constant. The pinning strength $k > 0$ has units of energy per length. Our main results do not depend on the details of E_{pin} . When an external magnetic field B is present we must also account for the dependence of its interaction with the spontaneous orbital magnetization on domain wall position,

$$dW_{\pm}^B = [-M_+X - M_-(-X)]WdB = -2MWX dB. \quad (9)$$

Here M_{\pm} is the net orbital moment per area of the \pm valley states and we used time reversal symmetry ($M_+ = -M_- \equiv M$) in the second equation. Introducing Eqs. (8) and (9) into Eq. (3) and integrating Eq. (6) over x yields:

$$\dot{\phi} = \frac{4AA_M}{\hbar\lambda} X'' + \frac{2A_MM B}{\hbar} - \frac{A_M k X}{\hbar} - \alpha_{\phi} \frac{\dot{X}}{\lambda}, \quad (10)$$

$$\frac{\dot{X}}{\lambda} = -\frac{2AA_M\pi}{\hbar} \phi'' + \frac{2K_{\perp}}{\hbar} \sin(2(\phi - \phi_p)) + \alpha_X \dot{\phi}. \quad (11)$$

Eq. (10) equates the precession frequency of the valley pseudospin to the wall-pressure generated by the sum of wall-curvature, magnetic-field, pinning forces, and damping forces. Note we distinguished α_X from α_{ϕ} since it requires processes that change overall valley polarization, and we therefore expect it to be much smaller. Indeed, α_{ϕ} has a substantial electronic contribution since [41] the Chern number change upon valley polarization reversal requires that the quasiparticle gap vanishes in the interior of the domain wall, see Fig. 1b). Eq. (11) is a continuity equation (with $K_{\perp} \rightarrow 0$) for valley-polarization expressed in collective coordinates: the damping term proportional to α_X is a valley-transfer torque that accounts for the valley-pumping quasiparticle currents generated by $\dot{\phi}$ [42–48].

So far we have not directly invoked the unusual physics of OCIs, except by allowing the valley polarization order parameter, which is important for identifying conjugate coordinates and therefore collective coordinate dynamics, and magnetization, which characterizes the strength of interactions with the external magnetic field, to be independent. For spin-magnets these two quantities have

a universal relationship characterized by the gyromagnetic ratio. The simple way in which transport currents influence domain wall dynamics, which we now explain, is however a very specific consequence of the topological character of OCIs.

The pinned domain wall in Fig. 2 separates orbital Chern insulator domains with opposite total Chern numbers. The domain wall therefore supports two co-propagating edge channels that are sourced entirely from different electrical contacts when tunneling between channels is negligible. We identify the local chemical potential difference between valleys on the domain wall with $\hbar\dot{\phi}$ via the Josephson-like voltage-frequency relationship [49]:

$$\hbar\dot{\phi} = \delta\mu \quad (12)$$

This fundamental relationship allows topological edge states to electrically control the properties of OCIs. Anticipating that substantial equilibration occurs in the hot-spot regions [50–52] indicated in Fig. 2 where the valley edge state channels meet near the sample boundary so that momentum is not-conserved, we set $\delta\mu = \gamma eV$, where $\gamma < 1$ is a fractional equilibration parameter.

Quasistatic-wall:– Eq. 10 has a quasistatic solution with ϕ and X independent of y , and X independent of time:

$$X_{\text{eq}} = \frac{2MB - A_M^{-1}\gamma eV}{k}. \quad (13)$$

Eq. (13) has the following thermodynamic interpretation. The chemical potential is the energy to add an electron to the system. In an ordinary insulator chemical potentials within the gap are undefined because the system is incompressible; no states are available to add electrons within the gap. In a Chern insulator, electrons can be added at energies within the gap, but only at an edge or a domain wall, and only by expanding the area of the system so that it holds one more electron. When a domain wall moves it adds electrons to one Chern insulator and removes it from the other. Eq. 13 places the domain wall at the position where the energy change for moving a domain wall by A_M/W , adding an electron to one domain and removing it from the other, is the chemical potential difference $\hbar\dot{\phi}$.

Reversal occurs at the depinning threshold $X_{\text{eq}} = X_{\text{max}}$. According to Eq. 13, the slope of the $X_{\text{eq}} = X_{\text{max}}$ line in the $(\delta\mu, B)$ parameter space is

$$\frac{d\delta\mu}{dB} = 2MA_M. \quad (14)$$

To relate reversal to the transport current we note that since two hot spots have been traversed the difference in local chemical potentials between top left and top right of the Hall bar in Fig. 2 is $\gamma^2 eV$. It follows that the net

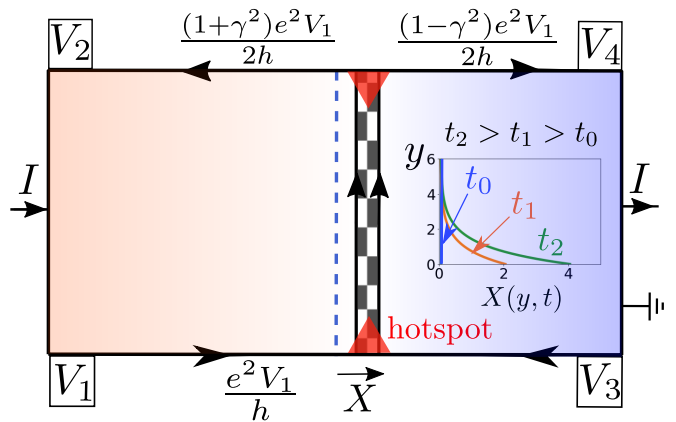


FIG. 2. Magnetization reversal in an orbital Chern insulator: A domain wall (vertical dashed line) separates the OCI into regions with opposite signs of the Hall conductances. Domain walls can be shifted (from 0 to X) and eventually depinned by a valley-dependent chemical potential $e(V_1 - V_3)$, or by a magnetic field. Inset shows bending of a domain wall close to a hot spot [55].

current flowing from source to drain is

$$I = V \frac{e^2}{h} \frac{1 - \gamma^2}{2} \quad (15)$$

and that reversal therefore occurs along a line in control parameter space with slope

$$\frac{dI}{dB} = MA_M \frac{e}{h} \frac{1 - \gamma^2}{\gamma}. \quad (16)$$

This is the central result of the paper. Since $MA_M \sim \mu_B$ in graphene multilayer OCIs [8] and $e\mu_B/h \sim 1.4 \times 10^{-8} \text{A/T}$ is two-orders of magnitude smaller than the experimental result reported in Ref. 6, this mechanism can apply to the samples studied experimentally only if $\gamma \sim 10^{-2}$, *i.e.* the edge channels are substantially equilibrated in the hot spot regions. This property is in fact consistent with reported observations [6]. Our theory of reversal can be tested quantitatively by measuring [53, 54] the longitudinal resistance along the upper edge of the Hall bar in Fig. 2 to determine a value for γ :

$$R = \frac{V_2 - V_4}{I} = \frac{2h}{e^2} \frac{\gamma^2}{1 - \gamma^2}. \quad (17)$$

Discussions:– When edge states arrive at a hotspot (cf. Fig. 2) with a valley (momentum) flux perpendicular to the domain wall, they can exert a force on the domain wall. If so, the wall will bend with a vertical profile satisfying Eq. (10)–(11), see Ref. 55. Illustrative wall profiles are shown in Fig. 2. Observation of such domain wall bending would support our proposed reversal mechanism.

Two interesting mechanisms for current reversal of orbital magnetization have recently been proposed in

Refs. 35 and 36. Their theories appeal to finite dissipation in the bulk ($\sigma_{xx} \neq 0$) and do not apply in the quantum anomalous Hall effect regime considered here. The theoretical analysis in Ref. [6] identifies an I^3 contribution (where I is the current) to the edge state free energy of conduction edge states and associated reversal with it becoming comparable to bulk magnetostatic energy. This reversal mechanism does not rely on wall dynamics. Our theory provides an alternative current-reversal mechanism based on depinning of valley domain walls via topological edge states and it is most relevant in devices with well defined orbital Chern insulators, like those imaged recently in Ref. [9].

Acknowledgement: The authors acknowledge informative interactions with Eli Fox, David Goldhaber-Gordon, Gregory Polshyn, Aaron Sharpe, and Andrea Young. This work was supported by DOE grant DE-FG02-02ER45958 and Welch Foundation grant TBF1473.

-
- [1] S. Bader and S. Parkin, “Spintronics,” *Annu. Rev. Condens. Matter Phys.*, vol. 1, no. 1, pp. 71–88, 2010.
- [2] S. Bhatti, R. Sbiaa, A. Hirohata, H. Ohno, S. Fukami, and S. Piramanayagam, “Spintronics based random access memory: a review,” *Materials Today*, vol. 20, no. 9, pp. 530–548, 2017.
- [3] V. Kruglyak, S. Demokritov, and D. Grundler, “Magnonics,” *Journal of Physics D: Applied Physics*, vol. 43, no. 26, p. 264001, 2010.
- [4] S. Roche, J. Åkerman, B. Beschoten, J.-C. Charlier, M. Chshiev, S. P. Dash, B. Dlubak, J. Fabian, A. Fert, M. Guimarães, *et al.*, “Graphene spintronics: the european flagship perspective,” *2D Materials*, vol. 2, no. 3, p. 030202, 2015.
- [5] A. L. Sharpe, E. J. Fox, A. W. Barnard, J. Finney, K. Watanabe, T. Taniguchi, M. Kastner, and D. Goldhaber-Gordon, “Emergent ferromagnetism near three-quarters filling in twisted bilayer graphene,” *Science*, vol. 365, no. 6453, pp. 605–608, 2019.
- [6] M. Serlin, C. Tschirhart, H. Polshyn, Y. Zhang, J. Zhu, K. Watanabe, T. Taniguchi, L. Balents, and A. Young, “Intrinsic quantized anomalous hall effect in a moiré heterostructure,” *Science*, vol. 367, no. 6480, pp. 900–903, 2020.
- [7] G. Chen, A. L. Sharpe, E. J. Fox, Y.-H. Zhang, S. Wang, L. Jiang, B. Lyu, H. Li, K. Watanabe, T. Taniguchi, *et al.*, “Tunable correlated chern insulator and ferromagnetism in trilayer graphene/boron nitride moiré superlattice,” *arXiv preprint arXiv:1905.06535*, 2019.
- [8] H. Polshyn, J. Zhu, M. A. Kumar, Y. Zhang, F. Yang, C. L. Tschirhart, M. Serlin, K. Watanabe, T. Taniguchi, A. H. MacDonald, *et al.*, “Nonvolatile switching of magnetic order by electric fields in an orbital chern insulator,” *arXiv preprint arXiv:2004.11353*, 2020.
- [9] C. Tschirhart, M. Serlin, H. Polshyn, A. Shragai, Z. Xia, J. Zhu, Y. Zhang, K. Watanabe, T. Taniguchi, M. Huber, *et al.*, “Imaging orbital ferromagnetism in a moiré chern insulator,” *arXiv preprint arXiv:2006.08053*, 2020.
- [10] R. Bistritzer and A. H. MacDonald, “Moiré bands in twisted double-layer graphene,” *Proceedings of the National Academy of Sciences*, vol. 108, no. 30, pp. 12233–12237, 2011.
- [11] Y. Cao, V. Fatemi, A. Demir, S. Fang, S. L. Tomarken, J. Y. Luo, J. D. Sanchez-Yamagishi, K. Watanabe, T. Taniguchi, E. Kaxiras, *et al.*, “Correlated insulator behaviour at half-filling in magic-angle graphene superlattices,” *Nature*, vol. 556, no. 7699, p. 80, 2018.
- [12] Y. Cao, V. Fatemi, S. Fang, K. Watanabe, T. Taniguchi, E. Kaxiras, and P. Jarillo-Herrero, “Unconventional superconductivity in magic-angle graphene superlattices,” *Nature*, vol. 556, no. 7699, pp. 43–50, 2018.
- [13] X. Lu, P. Stepanov, W. Yang, M. Xie, M. A. Aamir, I. Das, C. Urgell, K. Watanabe, T. Taniguchi, G. Zhang, *et al.*, “Superconductors, orbital magnets and correlated states in magic-angle bilayer graphene,” *Nature*, vol. 574, no. 7780, pp. 653–657, 2019.
- [14] M. Yankowitz, S. Chen, H. Polshyn, Y. Zhang, K. Watanabe, T. Taniguchi, D. Graf, A. F. Young, and C. R. Dean, “Tuning superconductivity in twisted bilayer graphene,” *Science*, vol. 363, no. 6431, pp. 1059–1064, 2019.
- [15] N. Nagaosa, J. Sinova, S. Onoda, A. H. MacDonald, and N. P. Ong, “Anomalous hall effect,” *Reviews of modern physics*, vol. 82, no. 2, p. 1539, 2010.
- [16] C.-Z. Chang, J. Zhang, X. Feng, J. Shen, Z. Zhang, M. Guo, K. Li, Y. Ou, P. Wei, L.-L. Wang, *et al.*, “Experimental observation of the quantum anomalous hall effect in a magnetic topological insulator,” *Science*, vol. 340, no. 6129, pp. 167–170, 2013.
- [17] K. He, Y. Wang, and Q.-K. Xue, “Topological materials: quantum anomalous hall system,” *Annual Review of Condensed Matter Physics*, vol. 9, pp. 329–344, 2018.
- [18] N. Bultinck, S. Chatterjee, and M. P. Zaletel, “Mechanism for anomalous hall ferromagnetism in twisted bilayer graphene,” *Physical Review Letters*, vol. 124, no. 16, p. 166601, 2020.
- [19] F. Wu and S. D. Sarma, “Collective excitations of quantum anomalous hall ferromagnets in twisted bilayer graphene,” *Physical Review Letters*, vol. 124, no. 4, p. 046403, 2020.
- [20] J. Liu and X. Dai, “Correlated insulating states and the quantum anomalous hall phenomena at all integer fillings in twisted bilayer graphene,” *Preprint at https://arxiv.org/abs/1911.03760*, 2020.
- [21] K. Kim, A. DaSilva, S. Huang, B. Fallahzad, S. Larentis, T. Taniguchi, K. Watanabe, B. J. LeRoy, A. H. MacDonald, and E. Tutuc, “Tunable moiré bands and strong correlations in small-twist-angle bilayer graphene,” *Proceedings of the National Academy of Sciences*, vol. 114, no. 13, pp. 3364–3369, 2017.
- [22] Y. Alavirad and J. D. Sau, “Ferromagnetism and its stability from the one-magnon spectrum in twisted bilayer graphene,” *arXiv preprint arXiv:1907.13633*, 2019.
- [23] C. Repellin, Z. Dong, Y.-H. Zhang, and T. Senthil, “Ferromagnetism in narrow bands of moiré superlattices,” *Physical Review Letters*, vol. 124, no. 18, p. 187601, 2020.
- [24] Y.-H. Zhang, D. Mao, and T. Senthil, “Twisted bilayer graphene aligned with hexagonal boron nitride: anomalous hall effect and a lattice model,” *Physical Review Research*, vol. 1, no. 3, p. 033126, 2019.
- [25] M. Xie and A. H. MacDonald, “Nature of the correlated insulator states in twisted bilayer graphene,” *Physical Review Letters*, vol. 124, no. 9, p. 097601, 2020.
- [26] Y.-H. Zhang, D. Mao, Y. Cao, P. Jarillo-Herrero, and

- T. Senthil, “Nearly flat chern bands in moiré superlattices,” *Physical Review B*, vol. 99, no. 7, p. 075127, 2019.
- [27] W. Heisenberg, *Two Lectures*, pp. 443–455. Berlin, Heidelberg: Springer Berlin Heidelberg, 1984.
- [28] F. London, “On the problem of the molecular theory of superconductivity,” *Physical Review*, vol. 74, no. 5, p. 562, 1948.
- [29] J. Jung, F. Zhang, and A. H. MacDonald, “Lattice theory of pseudospin ferromagnetism in bilayer graphene: Competing interaction-induced quantum hall states,” *Physical Review B*, vol. 83, no. 11, p. 115408, 2011.
- [30] K. Hejazi, X. Chen, and L. Balents, “Hybrid wannier chern bands in magic angle twisted bilayer graphene and the quantized anomalous hall effect,” *arXiv preprint arXiv:2007.00134*, 2020.
- [31] J. Zhu, J.-J. Su, and A. MacDonald, “The curious magnetic properties of orbital chern insulators,” *arXiv:2001.05084v4*, 2020.
- [32] A. Malozemoff and J. Slonczewski, *Magnetic Domain Walls in Bubble Materials: Advances in Materials and Device Research*, vol. 1. Academic press, 2016.
- [33] A. Hubert and R. Schäfer, *Magnetic domains: the analysis of magnetic microstructures*. Springer Science & Business Media, 2008.
- [34] P. Upadhyaya and Y. Tserkovnyak, “Domain wall in a quantum anomalous hall insulator as a magnetoelectric piston,” *Physical Review B*, vol. 94, no. 2, p. 020411, 2016.
- [35] Y. Su and S.-Z. Lin, “Switching of valley polarization and topology in twisted bilayer graphene by electric currents,” *arXiv:2002.02611*, 2020.
- [36] W.-Y. He, D. Goldhaber-Gordon, and K. Law, “Giant orbital magnetoelectric effect and current-induced magnetization switching in twisted bilayer graphene,” *Nature communications*, vol. 11, no. 1, pp. 1–8, 2020.
- [37] A. Kumar, M. Xie, and A. MacDonald, “In-preparation,”
- [38] L. Fritsche, J. Noffke, and H. Eckardt, “A relativistic treatment of interacting spin-aligned electron systems: application to ferromagnetic iron, nickel and palladium metal,” *Journal of Physics F: Metal Physics*, vol. 17, no. 4, p. 943, 1987.
- [39] H. Kronmüller, “General micromagnetic theory and applications,” *Materials Science and Technology*, pp. 1–43, 2006.
- [40] J. Slonczewski, “Dynamics of magnetic domain walls,” in *AIP Conference Proceedings*, vol. 5, pp. 170–174, American Institute of Physics, 1972.
- [41] V. Kamberský, “On ferromagnetic resonance damping in metals,” *Czechoslovak Journal of Physics B*, vol. 26, no. 12, pp. 1366–1383, 1976.
- [42] Y. Tserkovnyak, A. Brataas, G. E. Bauer, and B. I. Halperin, “Nonlocal magnetization dynamics in ferromagnetic heterostructures,” *Reviews of Modern Physics*, vol. 77, no. 4, p. 1375, 2005.
- [43] Y. Tserkovnyak, A. Brataas, and G. E. Bauer, “Enhanced gilbert damping in thin ferromagnetic films,” *Physical review letters*, vol. 88, no. 11, p. 117601, 2002.
- [44] M. Tsoi, A. Jansen, J. Bass, W.-C. Chiang, M. Seck, V. Tsoi, and P. Wyder, “Excitation of a magnetic multilayer by an electric current,” *Physical Review Letters*, vol. 80, no. 19, p. 4281, 1998.
- [45] D. C. Ralph and M. D. Stiles, “Spin transfer torques,” *Journal of Magnetism and Magnetic Materials*, vol. 320, no. 7, pp. 1190–1216, 2008.
- [46] J. C. Slonczewski *et al.*, “Current-driven excitation of magnetic multilayers,” *Journal of Magnetism and Magnetic Materials*, vol. 159, no. 1, p. L1, 1996.
- [47] L. Berger, “Emission of spin waves by a magnetic multilayer traversed by a current,” *Physical Review B*, vol. 54, no. 13, p. 9353, 1996.
- [48] J. Slonczewski, “Excitation of spin waves by an electric current,” *Journal of Magnetism and Magnetic Materials*, vol. 195, no. 2, pp. L261–L268, 1999.
- [49] L. Berger, “Possible existence of a josephson effect in ferromagnets,” *Physical Review B*, vol. 33, no. 3, p. 1572, 1986.
- [50] D. S. Wei, T. van der Sar, S. H. Lee, K. Watanabe, T. Taniguchi, B. I. Halperin, and A. Yacoby, “Electrical generation and detection of spin waves in a quantum hall ferromagnet,” *Science*, vol. 362, no. 6411, pp. 229–233, 2018.
- [51] H. Zhou, H. Polshyn, T. Taniguchi, K. Watanabe, and A. Young, “Solids of quantum hall skyrmions in graphene,” *Nature Physics*, vol. 16, no. 2, pp. 154–158, 2020.
- [52] S. Takei, A. Yacoby, B. I. Halperin, and Y. Tserkovnyak, “Spin superfluidity in the $\nu = 0$ quantum hall state of graphene,” *Phys. Rev. Lett.*, vol. 116, p. 216801, May 2016.
- [53] K. Yasuda, M. Mogi, R. Yoshimi, A. Tsukazaki, K. Takahashi, M. Kawasaki, F. Kagawa, and Y. Tokura, “Quantized chiral edge conduction on domain walls of a magnetic topological insulator,” *Science*, vol. 358, no. 6368, pp. 1311–1314, 2017.
- [54] I. T. Rosen, E. J. Fox, X. Kou, L. Pan, K. L. Wang, and D. Goldhaber-Gordon, “Chiral transport along magnetic domain walls in the quantum anomalous hall effect,” *npj Quantum Materials*, vol. 2, no. 1, pp. 1–6, 2017.
- [55] Supplementary-materials

Supplementary Materials: Current Driven Magnetization Reversal in Orbital Chern Insulators

In this supplementary material, we discuss the dynamics of orbital Chern insulator domain wall when an electric current pass through the system. As discussed in the maintext, the equation of motion for a domain wall located inside the pinning region is given by the following:

$$\dot{\phi}(y, t) = \frac{4AA_M}{\hbar\lambda} X''(y, t) + \frac{2A_M MB}{\hbar} - \frac{A_M k}{\hbar} X(y, t) - \alpha_\phi \frac{\dot{X}(y, t)}{\lambda}, \quad (\text{S1})$$

$$\frac{\dot{X}(y, t)}{\lambda} = -\frac{2AA_M\pi}{\hbar} \phi''(y, t) + \frac{2K_\perp}{\hbar} \sin 2(\phi(y, t) - \phi_p) + \alpha_X \dot{\phi}(y, t). \quad (\text{S2})$$

The equations above can be viewed as a dynamical system describing the time evolution of vector variable $\chi = (\phi, X/\lambda)^\text{T}$. In the absence of electric current, domain wall is static and the minimum wall energy configuration is described by the following fixed points:

$$\left(\phi^*, \frac{X^*}{\lambda} \right)^\text{T} = \left(\phi_p + \frac{n\pi}{2}, \frac{2MB}{k\lambda} \right)^\text{T} \equiv \chi^* \quad (\text{S3})$$

where $n \in \mathbb{Z}$.

When an electric current pass through an orbital Chern insulator with a domain wall (c.f. Fig. 2), it has to traverse along the domain wall by populating topologically protected edge states. We assume the current-carrying states arriving at the hotspot from contacts will partially equilibrate and enter the domain wall with a finite valley chemical potential $\delta\mu$. If so, $\delta\mu$ will precess valley pseudospin and drives domain wall into motion. We describe such wall dynamics by studying linear response around the fixed points: $\delta\chi \equiv \chi - \chi^*$. As discussed in the maintext, the edge state relaxation is concentrated at the hotspot which we locate at $y = 0$. Hence, we seek a solution of the form $\delta\chi \propto e^{-qy}$ where $q = 0$ correspond to the thermodynamic result discussed in the maintext. Linearizing Eq. (S1) and (S2) around the fixed points yield:

$$\hbar \frac{d}{dt} \begin{pmatrix} \delta\phi \\ \delta X/\lambda \end{pmatrix} = \frac{A_M}{1 + \alpha_X \alpha_\phi} \begin{pmatrix} 2\alpha_\phi(\pi A q^2 + (-1)^n K_\perp A_M^{-1}) & 4A q^2 - k\lambda \\ -2(\pi A q^2 + (-1)^n K_\perp A_M^{-1}) & \alpha_X(4A q^2 - k\lambda) \end{pmatrix} \begin{pmatrix} \delta\phi \\ \delta X/\lambda \end{pmatrix} \equiv R \cdot \delta\chi. \quad (\text{S4})$$

We tabulate the stability analysis around the fixed points in Table. 1. The rate matrix R has the following eigenvalues and eigenvectors:

$$\epsilon_\pm = \frac{a\alpha_\phi + b\alpha_X \pm \sqrt{a^2\alpha_\phi^2 + b^2\alpha_X^2 - 2ab(2 + \alpha_\phi\alpha_X)}}{2(1 + \alpha_\phi\alpha_X)}, \quad \mathbf{u}_\pm = (u_\pm, v_\pm)^\text{T} = \left(\frac{1 + \alpha_\phi\alpha_X}{a} \epsilon_\pm - \alpha_\phi, 1 \right)^\text{T}, \quad (\text{S5})$$

where $a = 2A_M(\pi A q^2 + (-1)^n K_\perp A_M^{-1})$ and $b = 4A_M A q^2 - k A_M \lambda$. Next, we construct a traveling domain wall from the superposition of \mathbf{u}_1 and \mathbf{u}_2 :

$$\chi(y, t) = \chi^* + \sum_{i=\pm} c_i \mathbf{u}_i e^{\epsilon_i t/\hbar - qy}, \quad (\text{S6})$$

where the coefficients c_\pm are determined from the initial conditions located at the hotspot:

$$\partial_t \chi(0, 0) = (\delta\mu/\hbar, v_0/\lambda)^\text{T}. \quad (\text{S7})$$

Here $\delta\mu = \gamma eV$ where $\gamma < 1$ is the hotspot equilibration parameter and eV is the voltage difference between the two contacts that sourced valley edge states. The initial velocity $v_0 = \dot{X}(0, 0)$ is a phenomenological parameter that depends on the microscopic details of the hotspot. From the initial conditions, we find

$$c_\pm = \frac{\delta\mu - \hbar v_0 \lambda^{-1} u_\mp}{u_\pm - u_\mp}, \quad (\text{S8})$$

and the wall position is given by

$$X(y, t) = X^* + \frac{\lambda e^{-qy}}{u_+ - u_-} \left[\delta\mu (e^{\epsilon_+ t/\hbar} - e^{\epsilon_- t/\hbar}) - \hbar v_0 \lambda^{-1} (u_+ e^{\epsilon_+ t/\hbar} + u_- e^{\epsilon_- t/\hbar}) \right]. \quad (\text{S9})$$

In Fig. 2 of the maintext, we plot the dynamics of vertical wall-profile from Eq. (S9) in the small time limit: $\delta X(y, t) = \tilde{v} t e^{-qy}$ where \tilde{v} is an effective wall velocity.

	Odd n	Even n
Strong Pinning ($k > 4Aq^2/\lambda$)	$\left\{ \begin{array}{l} \text{stable} \quad K_{\perp} > \pi Aq^2 \\ \text{unstable} \quad K_{\perp} < \pi Aq^2 \end{array} \right.$	unstable
Weak Pinning ($k < 4Aq^2/\lambda$)	unstable	unstable

TABLE I. Linear stability analysis. For even n , the dynamical system is generically unstable. When the pinning is weak $4Aq^2 > k\lambda$, the fixed points are unstable spirals or unstable nodes and when the pinning is strong $4Aq^2 < k\lambda$, the fixed points are saddle-points. For odd n fixed points with weak perpendicular anisotropy $\pi Aq^2 < K_{\perp}$, the dynamical stability is the same as even n fixed points. However, for odd n fixed points with strong perpendicular anisotropy $\pi Aq^2 > K_{\perp}$, the domain wall can either be a saddle point if pinning is weak $4Aq^2 > k\lambda$, or a stable fixed point if the pinning is strong $4Aq^2 < k\lambda$.